ELSEVIER

Available online at www.sciencedirect.com
SCIENCE DIRECT®

Coastal Engineering 49 (2003) 275–289

Coastal Engineering
An International Journal for Coastal, Harbour and Offshore Engineers

www.elsevier.com/locate/coastaleng

A video-based technique for mapping intertidal beach bathymetry

Stefan G.J. Aarninkhof [a,*], Ian L. Turner [b], Thomas D.T. Dronkers [c], Mark Caljouw [c], Leann Nipius [c]

[a] *WL/Delft Hydraulics, PO Box 177, 2600 MH Delft, The Netherlands*
[b] *Water Research Laboratory, School of Civil and Environmental Engineering, University of New South Wales, Sydney, Australia*
[c] *Delft University of Technology, Faculty of Civil Engineering and Geosciences, Delft, The Netherlands*

Received 28 February 2002; received in revised form 16 May 2003; accepted 13 June 2003

Abstract

Measuring the location of the shoreline and monitoring foreshore changes through time are core tasks carried out by coastal engineers for a wide range of research, monitoring and design applications. With the advent of digital imaging technology, shore-based video systems provide continuous and automated data collection, encompassing a much greater range of time and spatial scales than were previously possible using field survey methods.

A new video-based technique is presented that utilises full-colour image information, which overcomes problems associated with previous grey-scale methods, which work well at steep (reflective) sites, but are less successful at flatter (dissipative) sites. Identification of the shoreline feature is achieved by the automated clustering of sub-aqueous and sub-aerial pixels in 'Hue–Saturation–Value' (HSV) colour space, and applying an objective discriminator function to define their boundary (i.e., 'shoreline') within a time-series of consecutive geo-referenced images. The elevation corresponding to the detected shoreline features is calculated on the basis of concurrent tide and wave information, which is incorporated in a model that combines the effects of wave set-up and swash, at both incident and infragravity frequencies.

Validation of the technique is achieved by comparison with DGPS survey results, to assess the accuracy of the detection and elevation methods both separately and together. The uncertainties associated with the two sub-components of the model tend to compensate for each other. The mean difference between image-based and surveyed shoreline elevations was less than 15 cm along 85% of the 2-km study region, which corresponded to an horizontal offset of 6 m. The application of the intertidal bathymetry mapping technique in support of CZM objectives is briefly illustrated at two sites in The Netherlands and Australia.

Keywords: Video-based technique; Intertidal beach bathymetry; Hue–Saturation–Value

1. Introduction

Measuring the location of the shoreline and monitoring foreshore changes through time are core tasks carried out by coastal engineers at many sites around the world. The motivation may be research-oriented, but more often is associated with practical applica-

* Corresponding author. Tel.: +31-15-285-88-89; fax: +31-15-285-87-10.
E-mail address: Stefan.Aarninkhof@wldelft.nl (S.G.J. Aarninkhof).

0378-3839/$ - see front matter
doi:10.1016/S0378-3839(03)00064-4

tions that can include: identifying and quantifying shoreline erosion, assessment of the performance of coastal protection structures, and as a basic input to engineering design in the coastal zone.

Mapping of the shoreline and foreshore has traditionally relied upon conventional surveying methods and airphoto interpretation techniques. More recently, differential GPS has enabled the more rapid collection of shoreline and foreshore data in the field. With the recent advent of new digital imaging technology, shore-based video systems now provide the additional capability of automated data collection, encompassing a much greater range of time and spatial scales than were previously possible. Continuous (typically every daylight hour) collection of image data with a resolution of centimetres to meters, extending along regions of hundreds of meters to several kilometers, is now routinely undertaken at sites in the USA, Europe, Australia and Asia.

The high temporal and spatial resolution that these new image-based data provide is accompanied by new challenges. Fundamentally, the task is to first identify shoreline and foreshore features by the analysis of oblique images, and secondly to convert distorted image (two-dimensional) co-ordinates to their real-world (three-dimensional) position. The solution to the second problem is now well established, and is embedded in the Argus coastal imaging system (Holman et al., 1993; Aarninkhof and Holman, 1999) that underlies the work we present here.

The second challenge, of mapping the shoreline and foreshore from a time-series of digital images, is the focus of the paper. The development and validation of a new colour-based technique to map intertidal bathymetry is presented and discussed in some detail. The application of this technique at two sites in The Netherlands and Australia to support CZM objectives is briefly illustrated.

2. A new model to map intertidal beach bathymetry

2.1. Motivation

Models to quantify intertidal beach bathymetry from video imagery generally delineate a shoreline feature from oblique or plan view images and estimate the associated elevation from the hydrodynamic conditions at the time of image collection (e.g. Plant and Holman, 1997). This yields an alongshore elevation contour of the intertidal beach (Fig. 1). Mapping a time series of contour lines throughout the tidal cycle enables the composition of the beach surface between the shoreline contours at low and high tide, assuming changes of morphology to be small over the period of data sampling (typically 6–10 h).

The first generation of video-based shoreline detection techniques (e.g. Plant and Holman, 1997;

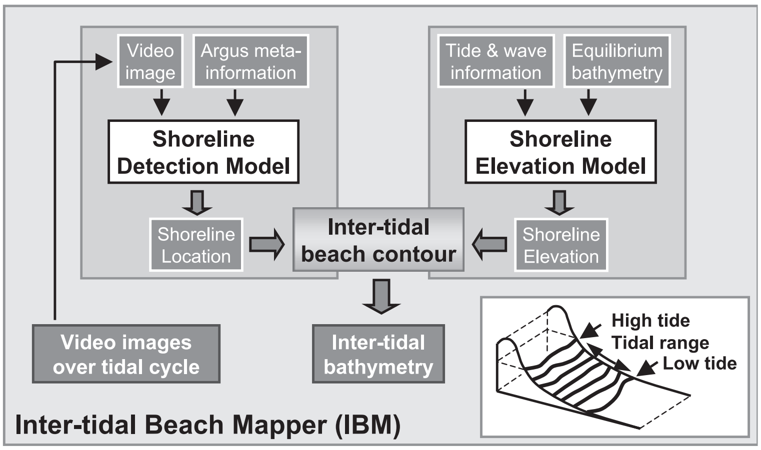

Fig. 1. Mapping intertidal beach bathymetry from a set of shorelines, derived from time-averaged video observations throughout a tidal cycle.

Aarninkhof et al., 1997; Davidson et al., 1997) originated from the time that Argus stations regularly collected grey-scale images only. These methods aimed to identify a characteristic pattern in the distribution of grey-scale pixel intensities sampled across the swash zone. The 'Shore-Line Intensity Maximum' (SLIM) model (Plant and Holman, 1997; Madsen and Plant, 2001) was typical of this approach, using the visually observed shoreline break as a proxy for the location of the shoreline. Application of the SLIM model was found to be highly robust, easy to automate and perform well at beaches with a well-pronounced and discrete SLIM feature.

These latter criteria occur at steep (reflective) beaches with mild to rough wave conditions. However, SLIM features are often diffuse or absent at mildly sloping (dissipative) beaches with emerging sandbars. This initiated the development of alternative shoreline detection techniques, which were still based upon grey-scale image information, but differed from the SLIM approach in that the location of the shoreline was estimated from a characteristic feature in the correlogram of the cross-shore intensity and variance profile (Aarninkhof et al, 1997) or spatial gradients in intensity levels in rectified images (Davidson et al., 1997). The absence of a well-pronounced greyscale contrast between pixel intensities sampled from sub-aerial and sub-aqueous regions of the beach often complicated or prevented unambiguous application of the latter techniques. A further difficulty with the grey-scale methods was that a site-dependent correction to estimate the shoreline elevation was generally required (e.g. Plant and Holman, 1997; Davidson et al., 1997).

The problems associated with the application of first generation shoreline detection models at mildly sloping beaches like Egmond (The Netherlands) and the Gold Coast (Queensland, Australia) has initiated the development of the new model presented here. Our technique identifies the shoreline location using the additional information made available by the use of full colour images. The horizontal position of the shoreline feature is obtained from the visual contrast between the sub-aqueous and sub-aerial beach, while the associated shoreline elevation is estimated from the offshore tide and wave conditions at the time of image collection. Both components of this new technique are summarised in Fig. 1, as described below.

2.2. Identification of the shoreline feature from video

A developmental version of the shoreline identification technique was previously described in Aarninkhof and Roelvink (1999). Briefly, the technique aims to delineate a shoreline feature from 10-min time exposure images, on the basis of distinctive image intensity characteristics in pixels, sampled across the sub-aqueous and sub-aerial beach, respectively. To that end, it converts raw image intensities in 'Red–Green–Blue' (RGB) colour space, sampled from a region of interest covering both the dry and wet beach, to 'Hue–Saturation–Value' (HSV) colour space, to separate colour (Hue, Saturation) and grey scale (Value) information (e.g. Russ, 1995). The HSV intensity data are filtered to remove outliers and scaled between 0 and 1, to improve the contrast between the two clusters of dry and wet pixels. Iterative low-pass filtering of the spiky histogram of scaled intensity data yields a smooth histogram with two well-pronounced peaks P_{dry} and P_{wet}, which mark the locations of the clusters of dry and wet pixels (Fig. 2a–b). The filtered histogram thus obtained is used to define a line l, formulated as

$$l\colon I_y = p_1 I_x + p_2 \tag{1}$$

where I_x and I_y represent Hue and Saturation in the case of colour-based discrimination (Fig. 2a), while both represent the Value information in the case of luminance-based discrimination (Fig. 2b). For both discriminators, the line l crosses the saddle point of the filtered histogram, thus separating the clusters of dry and wet pixels. When applied to an arbitrary image, the detection technique performs these operations in both the colour (Hue–Saturation) and luminance (Value–Value) domain and assesses what domain provides the highest degree of contrast between the sub-aqueous and sub-aerial beach. The latter is determined on the basis of a relative measure, involving the spread of pixel intensities within each cluster as regard to the distance between the cluster peak P and the discrimination line l.

With the help of l, a discriminator function $\Psi(I_x,I_y)$ is defined such that $\Psi = 0$ along l:

$$\Psi(I_x, I_y) = p_1 I_x + p_2 - I_y \tag{2}$$

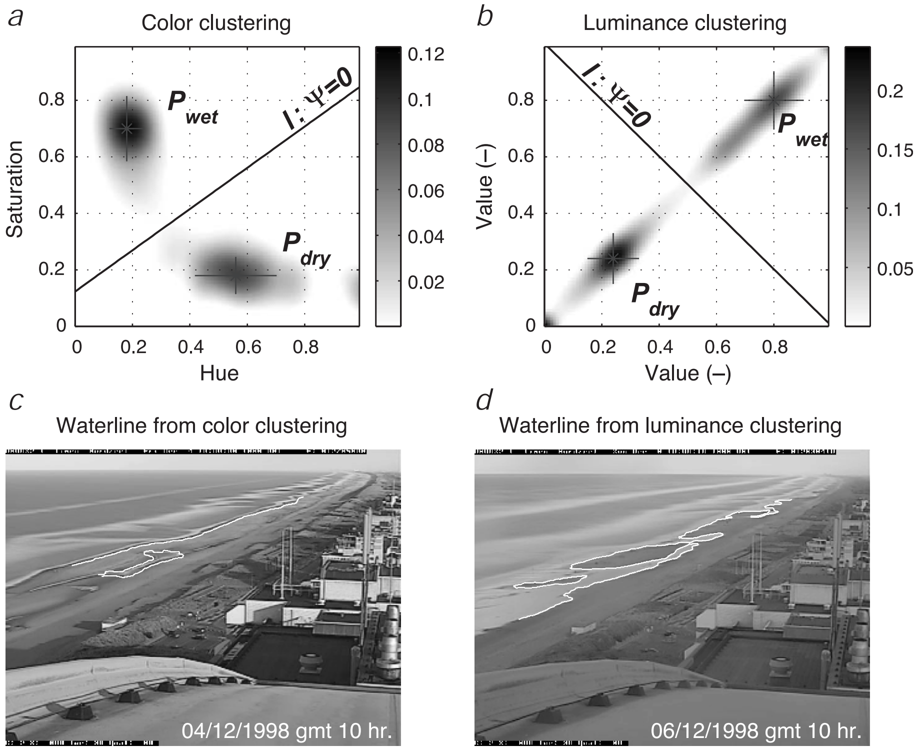

Fig. 2. Shoreline detection from contrasting pixel intensity characteristics at the sub-aqueous and sub-aerial beach. Video-based estimates of shoreline locations (c,d) at Noordwijk, Netherlands, determined from the clustering of pixel intensities in the colour (a) and luminance (b) domain, respectively.

Evaluation of Eq. (2) for the scaled intensity data (I_x,I_y) sampled from each individual pixel within the region of interest yields a map of the function Ψ, which shows positive (negative) Ψ at the sub-aerial (sub-aqueous) beach, for both colour-based and luminance-based cluster distinction. These maps enable the detection of the shoreline feature in image space at the location of the $\Psi=0$ elevation contour. Geo-referencing of this feature is achieved through application of sophisticated video-processing techniques (Holland et al., 1997). The result may locally show erroneous contours at the sub-aerial beach, which are associated with the irregular intensity characteristics of features like water-filled, detached runnel systems or vehicles at the beach. These are removed through application of empirical demands on shoreline persistency in both real world and image space. Example results representing colour-based and luminance-based shoreline detection at Noordwijk are shown in Fig. 2c–d, demonstrating the capability of this method to resolve three-dimensional morphology including emerging intertidal bars. An important attribute of this technique is that no site-specific calibration is required, and the method works equally well along reflective (steep) and more dissipative (flatter) coastlines.

2.3. Determination of the shoreline elevation at the time of image collection

During the 10 min of time exposure for image collection, the instantaneous location of the waterline (i.e. the interface of the sub-aerial and sub-aqueous beach) is affected by the offshore tidal level, storm surge, breaking induced wave set-up and swash oscillations (Fig. 3). As described above, the shoreline detection technique analyses time-averaged, colour video data to identify a beach contour at some location x_{sl} within the swash zone of width Δx_{osc} (i.e. the grey-

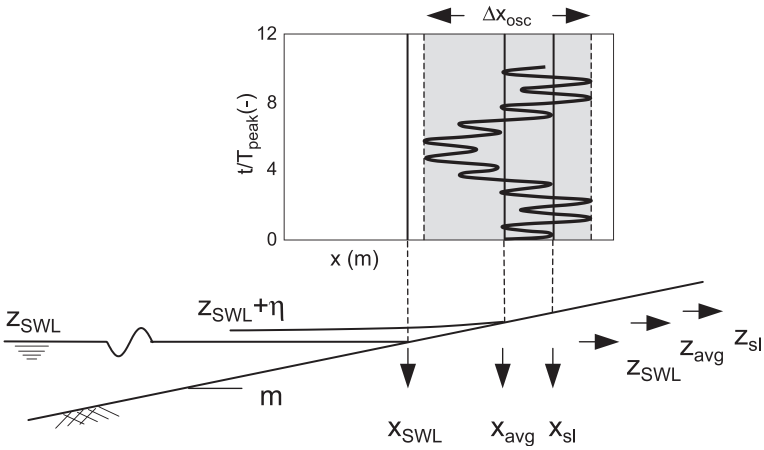

Fig. 3. Physical processes affecting the instantaneous waterline location. Artificial timestack of swash run-up a plane beach with slope m, for an energy spectrum dominated by short waves with peak period T_p and long waves with a period $7T_p$. The instantaneous waterline elevation z_{wl} is affected by the offshore water level z_o outside the surf zone, the breaking induced wave set-up η and an oscillatory component at the time scale of individual waves and wave groups.

shaded area in Fig. 3). In general, x_{sl} represents some (as yet unknown) location within the swash zone, which is associated with a certain level of swash exceedence. The elevation of this shoreline feature does not necessarily coincide with the 10-min time-averaged waterline location x_{avg} during this same time period.

The formulation for the water level elevation z_{sl} that corresponds to the horizontal position x_{sl} is defined by

$$z_{sl} = z_0 + \eta_{sl} + K_{osc}\frac{\eta_{osc}}{2} \quad (3)$$

where z_0 is the tide- and wind-induced offshore water level without the contribution of gravity waves, η_{sl} is the wave-breaking induced mean rise of the water level at the shoreline (hereafter referred to as wave set-up) and η_{osc} represents the vertical swash height, related to waterline oscillations at the time scale of individual waves and wave groups. The swash parameter K_{osc} is a constant, non-site-dependent empirical coefficient that accounts for the level of swash exceedence associated with the beach contour returned from the shoreline detection model.

The water level z_0 is preferably obtained within approximately 10 km off the coastline, so that variations of the tide and large-scale storm surge are measured, and local wind set-up between the tide gage and the shoreline is limited to a few centimetres. The wave set-up η_{sl} is computed from a standard wave decay model (Battjes and Janssen, 1978) that incorporates the roller concept (Svendsen, 1984; Stive and De Vriend, 1994) to delay the dissipation of organised energy. An inner surf zone bore model (Aarninkhof and Roelvink, 1999) is used to extend computations up to zero water depth.

To quantify the contribution of oscillations at incident (frequency f>0.05 Hz) and infragravity (f<0.05 Hz) frequencies to the overall swash height η_{osc} (Eq. (3)) at the shoreline, we adopt empirical formulations for the sea swell swash height R_{ss} and the infragravity swash height R_{ig}. Holman and Sallenger (1985) found the normalised infragravity swash height R_{ig}/H_0 and the normalised sea swell swash height R_{ss}/H_0 both to be linearly related to the Iribarren number ξ_0 as

$$\frac{R_{ig}}{H_0} = 0.53\xi_0 + 0.09 \quad (4a)$$

$$\frac{R_{ss}}{H_0} = 0.69\xi_0 - 0.19 \quad (4b)$$

where $\xi_0 = \tan(m)/\sqrt{H_0/L_0}$, m is the local foreshore slope and L_0 is the deep water wave length, determined with the peak period T_p. Eqs. (4a) and (4b) were derived for ξ_0 varying between $0.5<\xi_0<3.5$. Stockdon et al. (2002) confirm the general applicability of these empirical relationships over a range of reflective natural beaches. In contrast, at a low-sloping, dissipative beach at Terschelling (The Netherlands), Ruessink et al. (1998) found a significantly larger dependency between R_{ig}/H_0 and ξ_0, parameterised as

$$\frac{R_{ig}}{H_0}=2.20\xi_0+0.02 \tag{5}$$

The Ruessink et al. (1998) data set represents ξ_0 ranging between $0.05<\xi_0<0.35$. The increase of the constant of proportionality as compared to Eq. (4a) is ascribed to the saturation of the higher infragravity frequencies for situations with small ξ_0. To accommodate both dissipative and reflective conditions, Ruessink et al. (1998) suggest a relationship

$$\frac{R_{ig}}{H_0}=0.65\tanh(3.38\xi_0) \tag{6}$$

which reduces to Eq. (5) for highly dissipative conditions. For more reflective conditions, Eq. (6) converges to a constant value of 0.65, closely matching the relationship reported by Raubenheimer and Guza (1996), but underestimating the parameterisation according to Holman and Sallenger (1985) for $\xi_0>1.05$. To date, the validity of Eq. (6) in the transitional range between dissipative and reflective conditions has not been established because of a lack of measured data in the range $0.2<\xi_0$ 0.6. Pragmatically, being the only parameterisation for R_{ig} that caters for both dissipative and reflective conditions, it is adopted here for use with the shoreline elevation model.

In search of the quantification of R_{ss}, the shoreline elevation model adopts Eq. (4b) after Holman and Sallenger (1985). To prevent the occurrence of negative R_{ss}/H_0 as would be obtained for small ξ_0 outside the measured range of Holman and Sallenger, R_{ss}/H_0 is set to zero for calculated values of ξ_0 less than 0.275,

$$\frac{R_{ss}}{H_0}=0.69\xi_0-0.19 \quad \text{for } \xi_0>0.275 \tag{7a}$$

$$\frac{R_{ss}}{H_0}=0 \quad \text{for } \xi_0<0.275 \tag{7b}$$

thus, ignoring the short-wave contribution to swash oscillations during highly dissipative conditions ($\xi_0<0.275$). The latter can be justified from the measurements by Ruessink et al. (1998), where the average ratio of infragravity to total swash height R_{ig}/R was found to be 0.85. As both R_{ig} and R_{ss} are determined as a fraction of the offshore significant wave height H_0 defined as 4σ (where σ is the standard deviation of the sea surface elevation), the overall η_{osc} can be calculated as

$$\eta_{osc}=\sqrt{R_{ig}^2+R_{ss}^2} \tag{8}$$

where R_{ig} and R_{ss} are obtained from the empirical parameterisations (Eqs. (6)–(7b), respectively). The result obtained from Eq. (8) is used to estimate η_{sl} (Eq. (3)), applying the site-independent empirical constant K_{osc} to account for the level of swash exceedence associated with the beach contour obtained from the shoreline detection model.

3. Validation of the intertidal beach mapper

This section discusses the individual and combined validation of both sub-models that together comprise the intertidal beach mapper technique (Fig. 1), against a data set of GPS-surveyed shorelines sampled at Egmond, The Netherlands (Fig. 4).

3.1. Data set

A data set of 52 measured shorelines was collected at a nourished beach in front of the Egmond boulevard, during the periods November 29–30, 1999 and March 14–15, 2000. The shoreline surveys were conducted by moving a differential GPS system, mounted on a jeep, over a distance of approximately 2-km alongshore, at the higher part of the swash zone. These data yield a set of beach contours with a vertical accuracy of the order of 2 cm. The surveys were carried out on a semi-hourly basis, simultaneously to the recording of time-averaged video images by the five camera Argus video station, mounted at 43 m above sea level on top of the Egmond lighthouse 'Jan van Speyk' (Fig. 4). Offshore wave conditions (rms wave height H_{rms}, peak period T_p and angle of incidence θ_0) were measured

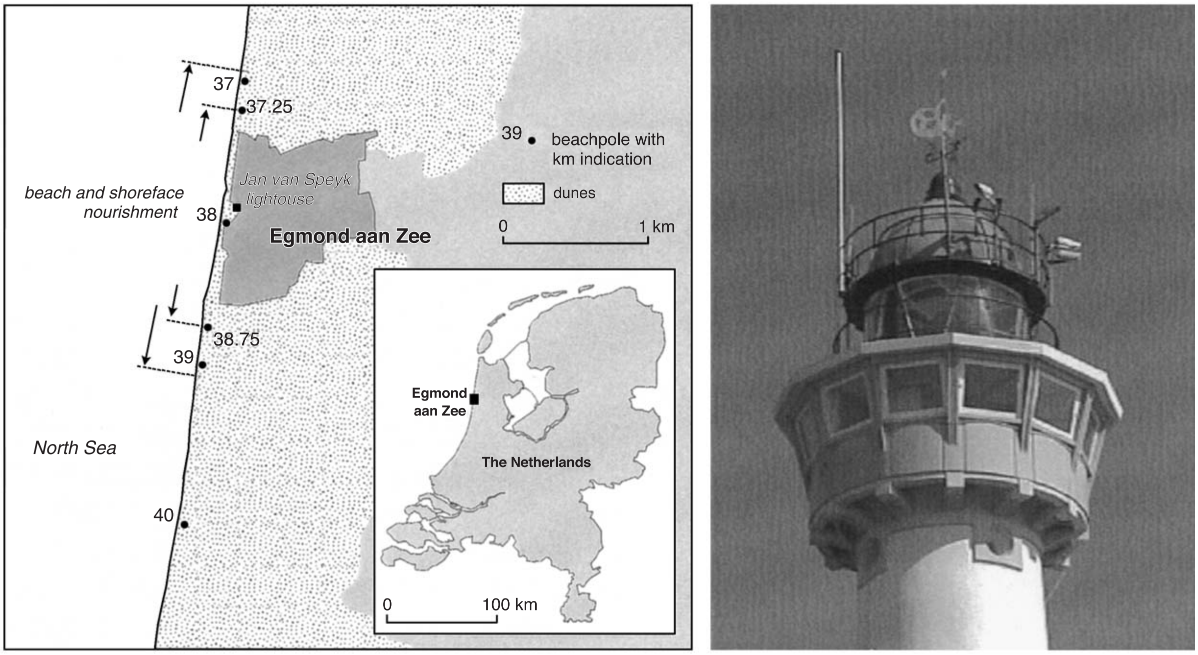

Fig. 4. Argus video station 'Jan van Speyk', mounted on top of the Jan van Speyk lighthouse in Egmond (Netherlands).

with a directional wave buoy at IJmuiden, located approximately 15 km to the south of the nourished site. Offshore tidal levels were interpolated using water level data collected at two tidal stations located 15 km north and south of Egmond. During the experiment, H_{rms} ranged between 0.6 and 2.3 m, while the offshore tidal level spanned a range between -0.7 and 1.0 m NAP (Dutch ordinance level).

The intertidal beach mapper was used to map shorelines from all 260 images collected simultaneously to the field measurements. On the basis of visual inspection (e.g. people on the beach, poor visibility, etc.), 137 shorelines were accepted for further analysis. Lacking information on the actual surf zone bathymetry, η_{sl} (Eq. (3)) was estimated by running the inner surf zone model on an equilibrium beach profile (Dean, 1977) calculated for the site. Previous investigations (Janssen, 1997) show that this simplification introduces only minor deviations of order 1–2 cm in terms of η_{sl} at the shoreline. The foreshore slope m at the intertidal beach was set at a fixed value 1:40, which is characteristic for the low gradient beach at Egmond. Deviations between the video-based and GPS surveyed shorelines are evaluated on a grid with 2 m spacing alongshore.

3.2. Error quantification

To separately assess the shoreline position and shoreline elevation sub-models (Fig. 1), deviations between modelled and surveyed shorelines were quantified by means of a horizontal offset δ_d, induced by the shoreline detection model, and a vertical offset δ_e, induced by the elevation model (Fig. 5),

$$\delta_d(y,t) = x_v(y,t) - x_s(y,t) \tag{9a}$$

$$\delta_e(y,t) = z_v(y,t) - z_s(y,t), \tag{9b}$$

where $x_v(y,t)$ and $x_s(y,t)$ represent the shoreline position x (positive offshore) at alongshore location y and time t, as identified from the video analysis and field survey, respectively. Similarly, $z_v(z_s)$ is the shoreline elevation obtained from video (field survey). To facilitate the inter-comparison, both deviations are interpreted as vertical offsets δz_d and δz_e, which demands the mapping of δ_d on a vertical plane with

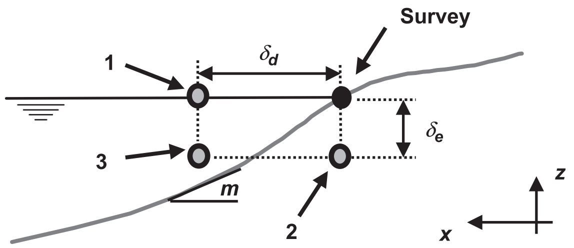

Fig. 5. Error quantification against GPS-surveyed shorelines. Quantification of model deviations by means of detection and elevation induced offsets δ_d and δ_e. Scenario 1 represents perfect performance of the elevation model, Scenario 2 represents perfect performance of the detection model and Scenario 3 the general case with non-zero δ_d and δ_e.

the help of the foreshore beach slope m, assuming m to be small such that $\tan(m) \approx m$:

$$\delta z_d(y,t) = m \times \delta_d(y,t) \tag{10a}$$

$$\delta z_e(y,t) = \delta_e(y,t) \tag{10b}$$

The overall error $\delta z(y,t)$ is determined as the sum of

$$\delta z(y,t) = \delta z_d(y,t) + \delta z_e(y,t) \tag{11}$$

Note that this approach allows the overall error δz to be smaller than the absolute values of the individual components δz_d and δz_e. This can be justified with the help of Fig. 5. In the case of a perfect estimate of the shoreline elevation (Scenario 1, $\delta z_e = 0$), δz is entirely governed by the detection induced error δz_d. In the case of perfect estimate of the shoreline location combined with a poor elevation estimate (Scenario 2), the opposite occurs. In general, both δz_d and δz_e will be non-zero. If δz_d and δz_e have opposite signs, this yields a decrease of the overall error δz, since errors resulting from both sub-models compensate for each other. This situation occurs for instance if a seaward offset of the video-derived location of the shoreline (positive δ_v) is compensated by an underestimate of the shoreline elevation (Scenario 3). The resulting δz is small as compared to the individual components δz_d and δz_e, which matches the real world situation where shoreline estimate 3 (Fig. 5) is much closer to the actual bathymetry than the estimates 1 and 2.

3.3. Assessment of model performance

The individual performance of the detection (elevation) model is quantified by means of the mean $\mu_{\delta z_d}$ ($\mu_{\delta z_e}$) and standard deviation $\sigma_{\delta z_d}$ ($\sigma_{\delta z_e}$) of δz_d (δz_e) over time, as function of the alongshore location y. The number of shorelines contributing to the statistics at an arbitrary location y^* varies with the location alongshore. Statistics were only determined if at least 10 shorelines were found in y^*, out of a theoretical maximum of 52. As a result, 4.3% of the grid points, all located in overlap regions between cameras or at the northern end of the area of interest, were excluded from the statistical analysis.

The results show negative $\mu_{\delta z_d}$ along virtually the entire area of interest (Fig. 6a), indicating that the horizontal position of video-derived shorelines were located landward of the surveyed shorelines. In absolute sense, the detection induced deviations $\mu_{\delta z_d}$ were generally less than 10 cm (with a relatively constant $\sigma_{\delta z_d}$ of about 15 to 20 cm) along the major part of the area of interest. The exception to this was in the far-field region to the north of the video station. Application of the elevation model (Fig. 6b) typically yielded mean deviations $\mu_{\delta z_e}$ up to 10 cm, with a $\sigma_{\delta z_e}$ in the order of 10 to 15 cm. The local increase of $\mu_{\delta z_e}$ and $\sigma_{\delta z_e}$ near $y = 800$ m was related to the presence of a local seaward morphological extension (clearly visible on plan view images of November 29, 1999), which induced a local increase of z_s, hence negative $\mu_{\delta z_d}$.

Similar trends were observed when considering the overall model performance in terms of the mean $\mu_{\delta z}$ and standard deviation $\sigma_{\delta z}$ of δz over time (Fig. 7). The tendency was for the absolute magnitude of the deviations to decrease, owing to the mutual compensation of errors resulting from the individual submodels. $\mu_{\delta z}$ typically amounted to 10–20 cm along the entire region of interest, except for the far-field region north of the video station where $\mu_{\delta z}$ locally increases up to 30 cm. In an absolute sense, $\mu_{\delta z}$ was less than 15 cm along 85% of the 2 km wide area of interest, which corresponded to an horizontal offset of 6 m. With $\sigma_{\delta z}$ in the order of 15 to 20 cm throughout most of the region of interest, the scatter of results is relatively constant, with larger values again found in the far-field region to the north and the non-uniform area near $y = 800$ m.

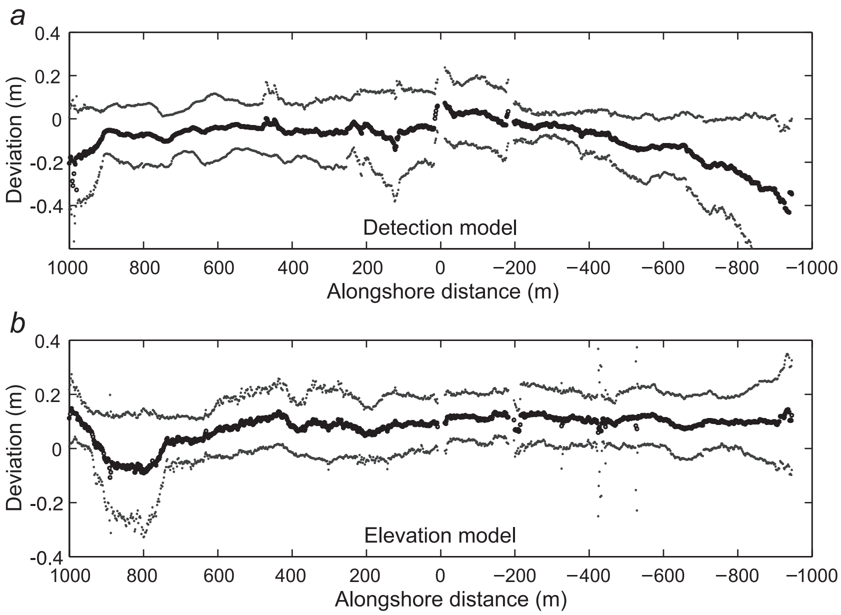

Fig. 6. Error quantification per sub-model. Time-averaged mean (bold dots) of the detection (a) and elevation model (b) induced vertical offsets δz_d and δz_e, as a function of the location alongshore. The fine dots represent the scatter, quantified as the mean ± the standard deviation of δz_d and δz_e. The positive y-axis is pointing south, with the video station being located around $y = -120$ m.

3.4. Sensitivity to the empirical swash parameter K_{osc}

The results presented here were obtained with a parameter setting $K_{osc} = 1.20$. To assess model sensitivity to variable K_{osc}, Table 1 summarises model performance for different K_{osc}, quantified by means of the rms error of the detection induced δz_d, the elevation induced δz_e and the overall offset δz, involving a total number of 29,551 samples that compose the entire data set of 137 video-based shorelines. The modelled mean shoreline elevation increased with increasing K_{osc}, yielding a decrease of the rms value of δz_e for K_{osc} ranging from 0.2 to 1. For K_{osc} above 1, the rms value of δz_e increased, indicating that the modelled shoreline elevation increasingly exceeded the surveyed elevation. However, the combined error, quantified by means of the rms value of δz, further decreased for K_{osc} values in exceedence of 1. This reflects the mechanism of mutual error compensation noted earlier. Minimum deviations in terms of δz are

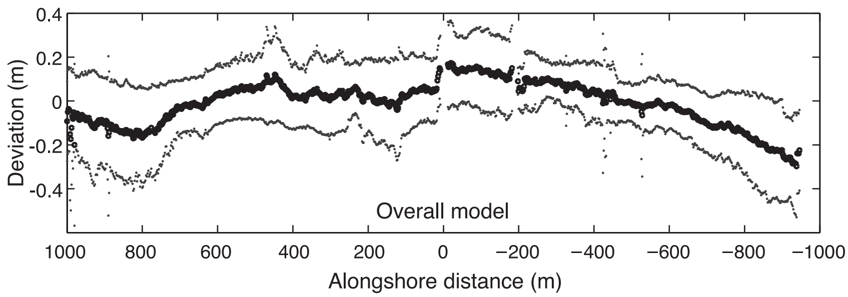

Fig. 7. Error quantification overall model. Time-averaged mean (bold dots) of the overall vertical offsets δz, as a function of the location alongshore. The fine dots represent the scatter, quantified as the mean ± the standard deviation of δz. The positive y-axis is pointing south, with the video station being located around $y = -120$ m.

Table 1
Sensitivity of the intertidal beach mapper to variable K_{osc}

K_{osc}	rms (δz_d)	rms (δz_e)	rms (δz)
0.20	0.194	0.209	0.318
0.50	0.194	0.153	0.259
0.80	0.194	0.122	0.211
1.00	0.194	0.125	0.190
1.20	0.194	0.148	0.182
1.40	0.194	0.182	0.188

obtained with a parameter setting $K_{osc}=1.2$, indicating that the detection technique identified a shoreline near the higher end of the swash run-up.

3.5. Discussion

Model validation against a data set of GPS surveyed shorelines at Egmond showed that mean vertical deviations, in absolute sense, were less than 15 cm (corresponding to a mean horizontal offset of 6 m) along more than 85% of the 2-km-long area of interest. Model deviations increased with increasing distance from the video station. The bulk statistics of the overall data set of 29,551 shoreline samples showed a mean, detection induced, vertical deviation of -8.5 cm (with standard deviation 17.4 cm), which reflects a landward offset of the video-derived shoreline location. This deviation is largely compensated by a mean elevation induced offset of $+7.8$ cm (with standard deviation 12.6 cm). Considering these standard deviations, it can be seen that the scatter of the overall model deviations was dominated by uncertainties resulting from the shoreline detection technique. The overall model deviations found here were the same order of magnitude as the vertical excursion of the oscillating swash motion, indicating that the technique was consistently identifying shorelines within the swash region.

The increase of $\mu_{\delta z_d}$ and $\sigma_{\delta z_d}$ with increasing distance from the video station can be explained by the discriminator function Ψ becoming less representative in the far-field of the rather large region of interest used for this comparison. The results presented here were obtained by sampling pixel intensities directly from oblique images. Owing to a decrease of the pixel resolution in the far-field, which is associated with less pixels per unit area, far-field information is relatively poorly represented. Consequently, the histogram of image intensities and the resulting discriminator function (Fig. 2) were biased towards the colour intensity characteristics of the near field. More difficult to control are atmospheric effects that increasingly affect image clarity, hence model performance, in the far-field. The decrease in model performance in the far-field to the north of the video station is further explained by the presence of buildings at the Egmond site, which obscure the visibility of the dry beach in this region, thus further limiting the opportunities for the clustering of dry pixels.

Apart from imperfections in the shoreline detection and elevation models as quantified above, the model accuracy reported here was also affected by the survey data. This observation concerns the survey method rather than the fundamental measurement accuracy of the differential GPS system (1–2 cm), which is an order of magnitude better than the image analysis technique described here. The elevation model assumes constancy of the time-averaged shoreline elevation during the 10-min of time exposure for image collection. So an ideal shoreline measurement would be surveyed along a perfectly horizontal track. This is hard to achieve in the field where the instantaneous location of the waterline is continually affected by oscillating swash motions over a complex intertidal bathymetry. The 137 GPS-surveyed shorelines that were used to quantify the offset of the corresponding 137 video-derived shorelines show a mean standard deviation of 4.7 cm. In other words, the scatter values $\sigma_{\delta z}$ reported here due to the image-based shoreline detection-elevation models represent the upper estimate of these errors, due to the inherent variability in the ground truth data.

The relatively large settings $K_{osc}=1.20$ found here indicates that the detection technique identifies a shoreline feature near the upper end of the swash run-up. However, this may also suggest that the empirical swash formulations which form the basis of the shoreline elevation model tend to underestimate the real-world vertical swash excursion. The latter may well be the case, as Eqs. (7a) and (7b) ignore the short-wave contribution R_{ss} at dissipative beaches ($\xi_0<0.275$). For reflective conditions characterised by $\xi_0>1.05$, the Ruessink et al. (1998) parameterisation for infragravity swash (Eq. (6)) underestimates the Holman and Sallenger (1985) relationship. Both aspects contribute to an underestimate of the real-world vertical swash excursion over a wide range of ξ_0, which is compensated by the large K_{osc} settings found here. It is concluded that the calibration of K_{osc} accounts for uncertainties in both the location of the shoreline feature identified from time-averaged video imagery as well as the associated elevation estimated from the empirical parameterisations for the vertical swash excursion.

4. Model application at Egmond and the gold coast

4.1. Video monitoring of a nourished beach at Egmond

To mitigate local beach erosion in front of the township of Egmond aan Zee (Fig. 4), the coastal authorities undertook combined beach and shoreface nourishment in the early summer of 1999. The 200 m^3/m beach nourishment extended a distance of 1500 m alongshore; the 400 m^3/m shoreface nourishment, completed at 5 m water depth at the seaward side of the outer bar, extended 2200 m. To monitor the effectiveness of the combined nourishment and its effect on the evolution of nearshore morphology, an Argus video station was installed on top of the 'Jan van Speyk' light house in May 1999. The intertidal beach mapper was used to quantify intertidal beach bathymetry on a monthly basis, between the NAP 0 and + 1 m elevation contours.

The initial intertidal morphology of June 1999, 2 months after the completion of beach and shoreface nourishment, was characterised by a highly irregular shoreline, with an erosion hot-spot located approximately 500 m south of the video station, and considerable accretion at 200 m north of the station (Fig. 8). The width of the beach varied of by more than 60 m within a distance of 700 m. After a calm summer period during which only minor foreshore changes were observed (Fig. 8), a sequence of storm events in October and November 1999 (upper panel, Fig. 8) causes significant erosion of the beach, in particular at the location of minimum beach width at about 400 m south of the video station (Fig. 8). The flattening of the beach profile was also observed, identified from the image-derived survey data by the widening of elevation contours. During the winter months (December 1999–February 2000), ongoing erosion was observed along the entire monitoring region. In March 2000, this had resulted in coastal retreat of 30 m in the north, and more than 40 m in the south. At some locations, virtually no sub-aerial beach was left, despite the nourishment activities which were executed only 9 months previously. Between April and June 2000, a degree of recovery (~ 20 m additional beach width) was observed; full restoration of the morphological configuration of June 1999 had however not been achieved.

A second beach nourishment was completed by the end of June 2000, along the strip between 0 and 800 m south of the video station. Shoreline retreat of 10–20 m per month continued along the nourished section over the period August–September 2000, as the nourished sand transferred from the intertidal beach to restore an erosion hot-spot around 700 m south of the video station (Fig. 8). Rough wave conditions (upper panel, Fig. 8) in November and December 2000 resulted in further erosion, and a shoreward shift of the shoreline by 15–20 m, relative to the initial beach conditions measured in June 1999. Early in 2001, a 'slug' of sand entered the intertidal zone directly north of the video station (Fig. 8), causing a net local accretion in the order of 50 m, accompanied by the flattening of the beach profile and the development of strong morphological irregularities in the intertidal zone. The redistribution of sediments alongshore, combined with an overall accretionary trend, resulted in an increasingly smoothed shoreline in April 2001 with this trend continuing through to end of the summer in August 2001. Interestingly, the plan-shape morphological configuration of August 2001, characterised by a seaward extension of the foreshore directly north of the video station, and a contrasting erosion hot-spot approximately 600 m to the south, is remarkably similar to the initial situation in June 1999, despite the nourishment effort in July 2000. This latter observation suggests that the morphological evolution of the intertidal beach is at least partly governed by larger-scale phenomena, for example the presence of a depression in the outer bar.

In summary, 2 years of video-based monitoring of intertidal coastal changes at a nourished beach on the west coast of The Netherlands have shown significant variability in the morphodynamic behaviour at the site. Averaged over the area of interest, a strong seasonal variability was observed, and considerable spatial variability occurred through redistribution of sedi-

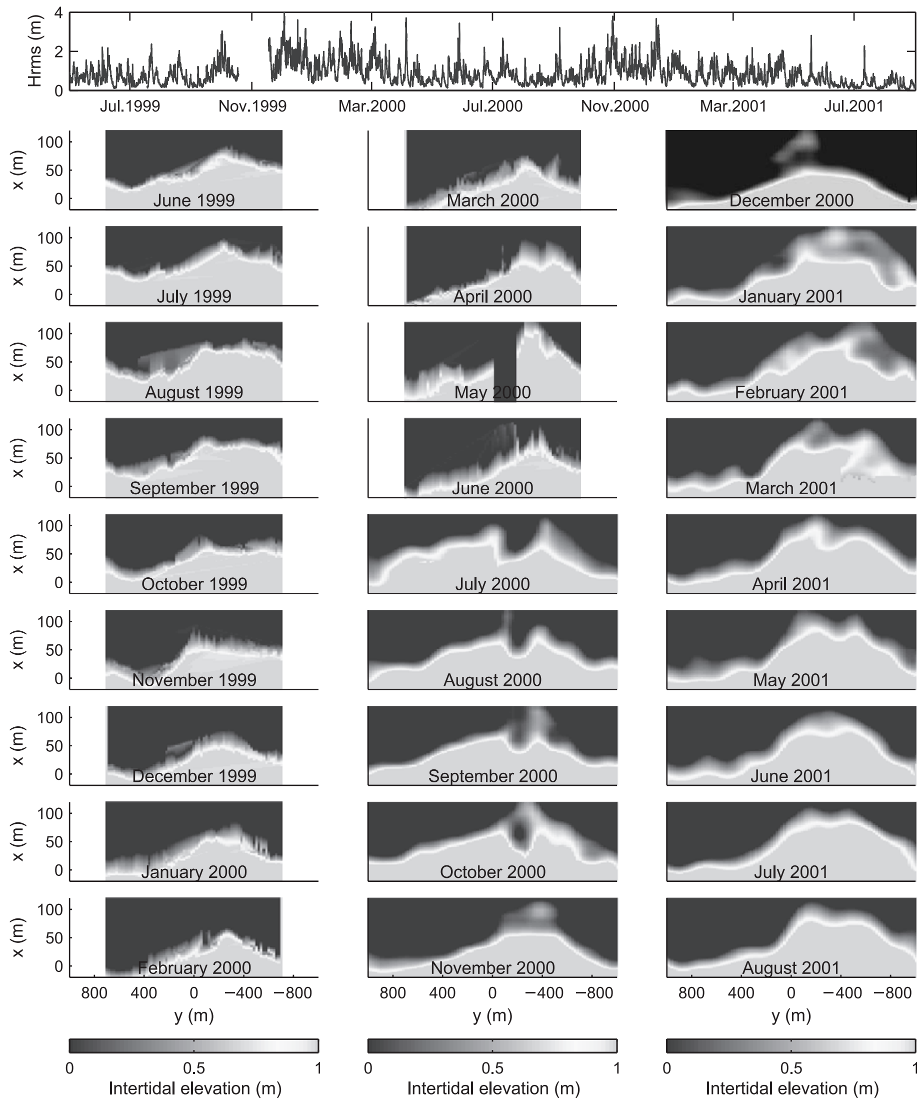

Fig. 8. Video-observed evolution of intertidal bathymetry at Egmond over the period June 1999 – August 2001. Monthly, plan view maps of the intertidal beach bathymetry between the NAP + 0 and NAP + 1 m elevation contours. The dry beach is located at the lower side of each panel. The video station is located near the origin of the horizontal coordinate axis, which is positively directed south. Elevations at the sub-aqueous (sub-aerial) beach are manually set to zero (one). The upper panel shows H_{rms} for the period of interest.

ments within the area of interest. In the past, this variability had the effect of obscuring a (previously unrecognised) chronic erosion problem in the southern region of the monitored area. This had resulted in the design and implementation of an inappropriate coastal management option (i.e., sand nourishment). The application of the intertidal beach mapper technique at the site clearly identified and located the underlying chronic erosion problem, and is contributing to the design of more effective mitigation measures.

4.2. Video monitoring of coastal changes at the Gold Coast Reef (Australia)

In 1997, the 'Northern Gold Coast Beach Protection Strategy' (Boak et al., 2000) was implemented by Gold Coast City Council to maintain and enhance the beaches extending from Surfers Paradise to Main Beach (Fig. 9). The aim of the Strategy was to decrease the risk of potential economic loss (infrastructure and tourism) following storms events, by increasing the volume of sand within the storm buffer seaward of the existing oceanfront boulder wall. The Strategy has the dual objectives of increasing the width of the sub-aerial beach, and improved surfing conditions. The major components of the engineering works included an initial 1.2 Mm^3 of beach nourishment along approximately 2000 m of the coastline, and construction at Narrowneck (Fig. 9) of a submerged artificial reef structure to provide a coastal 'control point' and enhance surfing opportunities. In August 1999, an Argus coastal imaging system was installed at the site, immediately prior to the start of reef construction, and 6 months following the commencement of beach nourishment.

Within the scope of a larger video-based monitoring program (Turner et al., in press), the intertidal beach mapper technique was applied to assess foreshore morphological changes during the construction phase of the submerged reef structure. Intertidal beach profiles were mapped on a monthly basis over the 18-month period January 2000 to August 2001. The area of interest focussed on a 1000-m length of the beach, centered at the reef construction site. In contrast to the presentation of monthly intertidal beach profiles as shown for the Egmond site (Fig. 8), a quarterly summary of relative changes in the intertidal beach profile can also be calculated (Fig. 10) to assess the alongshore distribution of accretion–erosion.

In July 2000, sand nourishment of northern Gold Coast beaches was completed, and the video-derived results shown in Fig. 10 were calculated relative to the beach at that time, encompassing the subsequent 12-month period. An initial phase of accretion was observed to have occurred in the region between 600 and 1100 m alongshore, coinciding with a period of relatively calm waves. After than time, it was observed that sand generally migrated northwards, leaving behind a localised region of accretion in the lee and immediately up-drift of the reef structure (Fig. 10). The alongshore migration speed

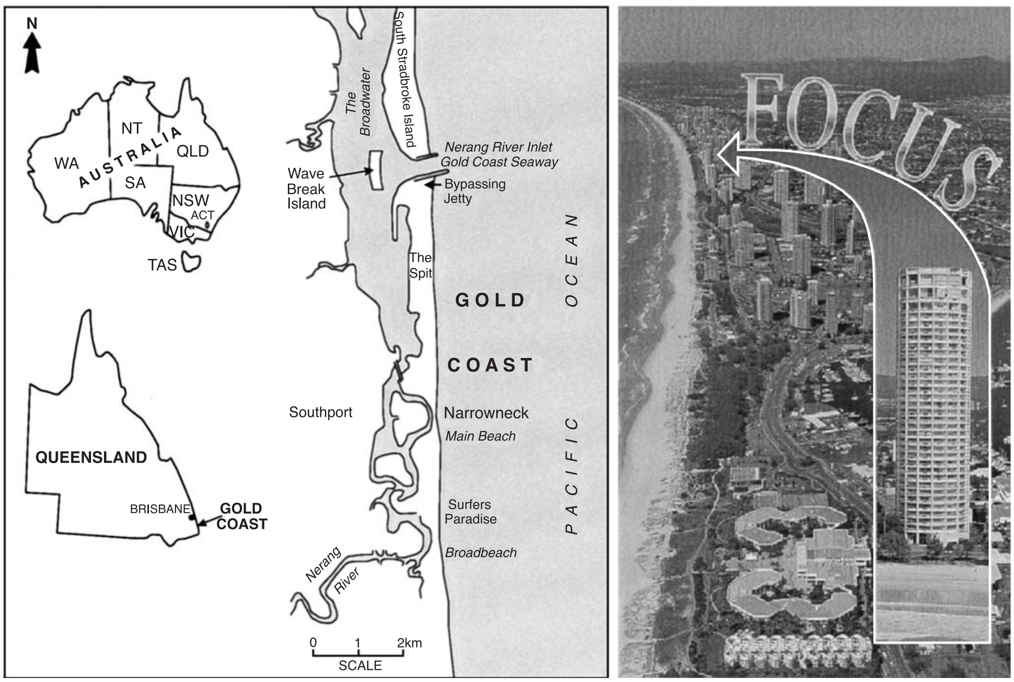

Fig. 9. The Goldcoast Argus video station, mounted on top of the Focus building at Narrowneck (Queensland, Australia).

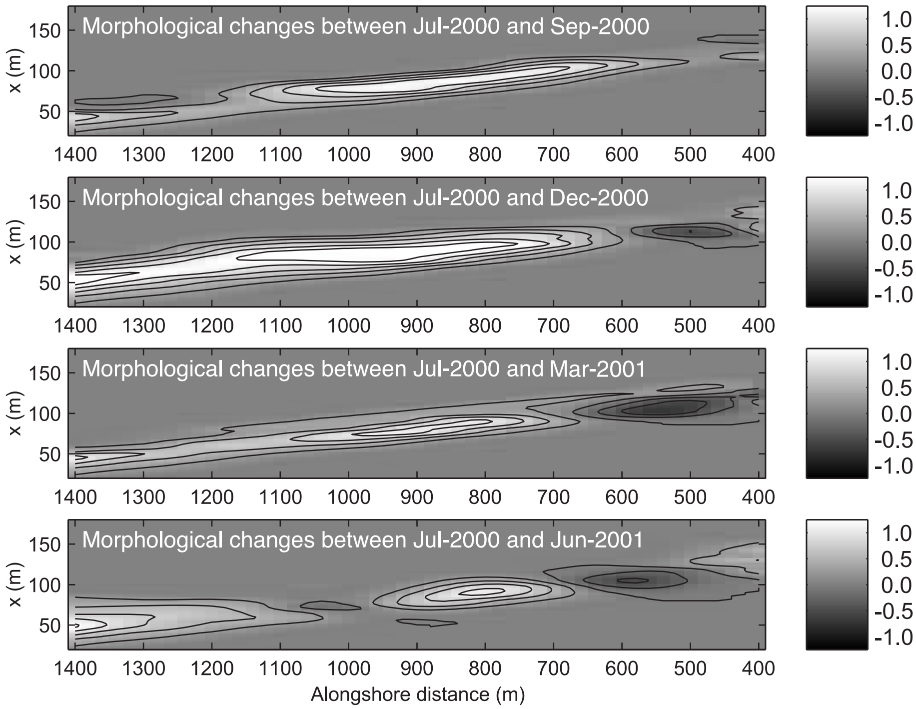

Fig. 10. Video-observed evolution of intertidal bathymetry at the Gold Coast over the period July 2000–June 2001. Quarterly maps of coastal changes at the intertidal beach, relative to the coastal morphology at the time of completion of the beach nourishment. The dry beach is located at the lower side of each panel. The video station is located near the origin of the horizontal coordinate axis, which is positively directed north.

was estimated based upon the monthly accretion–erosion calculations. By this method a net migration speed of ~ 1 m/day was determined for calm weather conditions (Hs ~ 1 m during September 2000–December 2000) and about 8 m/day for rough weather conditions (Hs ~ 2 m during December 2000–February 2001). It is interesting to note that these estimates of the migration speed using the video-derived estimates of foreshore accretion–erosion (Fig. 10) correspond well with the simple empirical approach proposed by Sonu (1968). By this method, the predicted average annual migration speed for this same 12-month period was approximately 6 m/day.

In summary, video-based monitoring of reef construction and nourishment works at a dissipative site on the east coast of Australia, has provided coastal managers the ability to assess and quantify the effectiveness of the new coastal protection works to meet project objectives. The application of the intertidal beach mapper technique is continuing to be used at the site on an ongoing basis, to determine when additional nourishment will be required.

5. Conclusions

This paper has presented the details and validation of a video-based method for monitoring of morphological changes at the intertidal beach.

The quantification of intertidal beach bathymetry is achieved by mapping multiple shorelines during a tidal cycle. The technique presented here is based upon two independent sub-models. The first identifies the location of the shoreline from time-averaged video images, based on colour differences between the wet and dry beach. The second estimates the associated vertical elevation from the hydrodynamic conditions offshore. These sub-models were validated separately, indicating that the waterline detection sub-model is largely responsible for deviations between the video-based waterline and the GPS-surveyed waterline. Uncertainties of the overall model are typically in the order of 15 cm in the vertical sense, which is of the same order of magnitude as the dimensions of the swash zone. From this validation, it can be concluded that the model is well suited for monitoring intertidal beach changes at the time scale of weeks to months.

Application of the model to two different Argus stations at Egmond and the Northern Gold Coast have shown significant morphological changes in the intertidal beach, which can be related to seasonal variability, placing of nourishment, storm-based erosion events and the construction of a reef respectively. The observed evolution of the intertidal beach indicates variability on relatively short temporal and spatial scales, which are not easily observed with more traditional field methods.

Acknowledgements

This study was funded by the Interfaculty Research Centre 'Observation of the Earth and Earth's crust' at Delft University of Technology, the Dutch Ministry of Transport and Public Works (Rijkswaterstaat). The Argus station at the Gold Coast is funded by Gold Coast City Council. SGJA and TDTD were co-sponsored by the Delft Cluster Project Coasts (03.01.03) and the EU-funded CoastView project (contract number EVK3-CT-2001-0054). ILT collaborated in the preparation of the revised manuscript while working as a guest at WL/Delft Hydraulics. The Argus video technique has been developed with funds generated by the Coastal Imaging Laboratory, Oregon State University. The authors wish to acknowledge Prof. Rob Holman, OSU, for actively and generously stimulating the collaboration within the worldwide Argus research group.

References

Aarninkhof, S.G.J., Holman, R.A., 1999. Monitoring the nearshore with video. Backscatter 10 (2), 8–11.

Aarninkhof, S.G.J., Roelvink, J.A., 1999. Argus-based monitoring of intertidal beach morphodynamics. Proc. of Coastal Sediments Conf., Long Island (NY), USA, pp. 2429–2444.

Aarninkhof, S.G.J., Janssen, P.C., Plant, N.G., 1997. Quantitative estimations of bar dynamics from video images. Proc. Coastal Dynamics Conf., Plymouth, UK, pp. 365–374.

Battjes, J.A., Janssen, J.P.F.M., 1978. Energy loss and set-up due to breaking in random waves. Proc. of 16th Int. Conf. on Coastal Eng. ASCE, New York, pp. 569–587.

Boak, L., McGrath, J., Jackson, L.A., 2000. IENCE—a case study—the Northern Gold Coast Beach protection strategy. Proc. of 27th Int. Conf. on Coastal Eng., vol. 4. ASCE, Sydney, pp. 3710–3717.

Davidson, M., Huntley, D., Holman, R., George, K., 1997. The evaluation of large scale (km) intertidal beach morphology on a macrotidal beach using video images. Proc. Coastal Dynamics Conf., Plymouth, UK, pp. 385–394.

Dean, R.G., 1977. Equilibrium beach profiles: US Atlantic and Gulf coast. Ocean Engineering Report, vol. 12. University of Delaware, Newark, DE. 45 pp.

Holland, K.T., Holman, R.A., Lippmann, T.C., Stanley, J., Plant, N.G., 1997. Practical use of video imagery in nearshore oceanographic field studies. IEEE Journal of Oceanic Engineering 22 (1), 81–92.

Holman, R.A., Sallenger Jr., A.H., 1985. Setup and swash on a natural beach. Journal of Geophysical Research 90, 945–953.

Holman, R.A., Sallenger Jr., A.H., Lippmann, T.C., Haines, J.W., 1993. The application of video image processing to the study of nearshore processes. Oceanography 6 (3).

Janssen, P.C., 1997. Intertidal beach level estimations from video images. MSc. Thesis. Delft University of Technology, Faculty of Civil Engineering and Geosciences.

Madsen, A.J., Plant, N.G., 2001. Intertidal beach slope predictions compared to field data. Marine Geology 173, 121–139.

Plant, N.G., Holman, R.A., 1997. Intertidal beach profile estimation using video images. Marine Geology 140, 1–24.

Raubenheimer, B., Guza, R.T., 1996. Observations and predictions of wave run-up. Journal of Geophysical Research 101, 25575–25587.

Ruessink, B.G., Kleinhans, M.G., Van Beukel, P.G.L., 1998. Observations of swash under highly dissipative conditions. Journal of Geophysical Research 103, 3111–3118.

Russ, J.C., 1995. The Image Processing Handbook, 2nd ed. Boca Raton (Florida), USA. CRC Press (ISBN 0-8493-2516-1).

Sonu, C.J., 1968. Collective movement of sediment in littoral environment. Journal of Coastal Engineering, 373–400 (Chapter 24).

Stive, M.J.F., De Vriend, H.J., 1994. Shear stresses and mean flow in shoaling and breaking waves. Proc. Int. Conf. Coastal Eng. ASCE, New York, pp. 594–608.

Stockdon, H.F., Holman, R.A., Sallenger Jr., A.H., 2002. Parameterisation of incident and infragravity swash variance. Eos Trans. AGU, vol. 83 (47), p. F746. Fall Meet. Suppl.

Svendsen, I.A., 1984. Wave heights and set-up in a surf zone. Coastal Engineering 8, 303–329.

Turner, I.L., Aarninkhof, S.G.J., Dronkers, T.D.T., McGrath, J., in press. CZM applications of Argus coastal imaging at the Gold Coast, Australia. Journal of Coastal Research.